

1 Revision 2

2 **The effects of ferromagnetism and interstitial hydrogen on the**
3 **equation of states of hcp and dhcp FeH_x: Implications for the Earth's**
4 **inner core age**

5 Hitoshi Gomi ^{a,b,*}, Yingwei Fei ^a, Takashi Yoshino ^b

6 ^aGeophysical Laboratory, Carnegie Institution of Washington, Washington, District of
7 Columbia 20015-1305, USA.

8 ^bInstitute for Planetary Materials, Okayama University, Misasa, Tottori 682-0193,
9 Japan.

10 * Corresponding author. *E-mail address*: hitoshi.gomi@okayama-u.ac.jp

11

ABSTRACT

12

13 Hydrogen has been considered as an important candidate of light elements in the Earth's
14 core. Because iron hydrides are unquenchable, hydrogen content is usually estimated
15 from in-situ X-ray diffraction measurements assuming the following linear relation: $x =$
16 $(V_{\text{FeH}_x} - V_{\text{Fe}}) / \Delta V_{\text{H}}$, where x is the hydrogen content, ΔV_{H} is the volume expansion
17 caused by unit concentration of hydrogen, V_{FeH_x} and V_{Fe} are volumes of FeH_x and pure
18 iron, respectively. To verify the linear relationship, we computed the equation of states
19 of hexagonal iron with interstitial hydrogen by using the Korringa-Kohn-Rostoker
20 method with the coherent potential approximation (KKR-CPA). The results indicate a
21 discontinuous volume change at the magnetic transition and almost no compositional (x)
22 dependence in the ferromagnetic phase at 20 GPa, whereas the linearity is confirmed in
23 the non-magnetic phase. In addition to their effects on density-composition relationship
24 in the Fe- FeH_x system, which is important for estimating the hydrogen incorporation in
25 planetary cores, the magnetism and interstitial hydrogen also affect the electrical
26 resistivity of FeH_x . The thermal conductivity can be calculated from the electrical
27 resistivity by using the Wiedemann-Franz law, which is a critical parameter for
28 modeling the thermal evolution of the Earth. Assuming an $\text{Fe}_{1-y}\text{Si}_y\text{H}_x$ ternary outer core
29 model ($0.0 \leq x \leq 0.7$), we calculated the thermal conductivity and the age of the inner
30 core. The resultant thermal conductivity is ~ 100 W/m/K and the maximum inner core
31 age ranges from 0.49 to 0.86 Gyr.

32 Keywords: FeH_x ; ferromagnetism; chemical disorder; equation of states; KKR-CPA;

33

INTRODUCTION

34

35 Seismologically inferred density profile of the Earth interior suggests that some
36 amounts of light alloying elements are incorporated into iron-based metallic core (Birch,
37 1964). Hydrogen is one of the important light element candidates in the Earth's core,
38 because only a small amount of interstitial hydrogen may drastically change the
39 physical properties of iron at high pressure, e.g. crystal and magnetic structure (e.g.
40 Isaev et al., 2007; Elsässer et al. 1998; Pépin et al., 2014), melting temperature (e.g.
41 Yagi and Hishinuma, 1995; Okuchi, 1998; Sakamaki et al., 2009; Shibazaki et al., 2011;
42 2014), density and elastic properties (Caracas, 2015; Hirao et al., 2004; Mao et al.,
43 2004; Pépin et al., 2014; Shibazaki et al., 2012; Tagawa et al., 2016; Umemoto and
44 Hirose, 2015). The maximum abundance of hydrogen has been estimated to be $0.3 \leq x \leq$
45 0.5 (in atomic ratio) for the Earth's core (Okuchi, 1997; Narygina et al., 2011; Umemoto
46 and Hirose, 2015). Furthermore, recent experimental study on hcp Fe-Si-H ternary
47 alloys suggests that the abundance of alloying hydrogen is $x = 0.17$ (Tagawa et al.,
48 2016). These results rely on our knowledge of non-stoichiometric phases such as FeH_x .

49 Investigation of non-stoichiometric FeH_x is not an easy task for both experimental
50 and theoretical studies. Experimental measurements on non-stoichiometric FeH_x alloys
51 have been very limited (Yamakata et al., 1992; Antonov et al., 1998; Shibazaki et al.,
52 2014; Machida et al., 2014; Tagawa et al., 2016; Iizuka-Oku et al., 2017), because most
53 of the previous experiments on Fe-H system were conducted under hydrogen-saturated
54 conditions. On the other hand, theoretical studies have the advantage of simulating
55 non-stoichiometric FeH_x alloys by means of super-cell technique (e.g. Caracas, 2015;
56 Umemoto and Hirose, 2015). However, such method requires large super cell to

57 calculate arbitrary concentration of hydrogen. Furthermore, the calculated results are
58 influenced by the geometry of the super cell (Caracas, 2015).

59 Here we report results of the total energy and the band structure of FeH_x alloys
60 obtained by means of first-principles calculations based on the Korringa-Kohn-Rostoker
61 method (KKR) (e.g. Akai, 1989). The coherent potential approximation (CPA) is
62 adopted to deal with the alloying effect, which is a complementary approach to the
63 super-cell method. In this study, we focused on the equation of state (EoS) of hexagonal
64 close-packed (hcp) and double hexagonal close-pack (dhcp) iron hydrogen alloys FeH_x ,
65 in order to evaluate the effect of ferromagnetism and interstitial hydrogen. The results
66 demonstrate the non-linear volume change with hydrogen content due to magnetic
67 transition. We will discuss on the validity of estimation of hydrogen content by in situ
68 X-ray diffraction. Another pronounced feature of the CPA is the explicit representation
69 of broadening of band structure due to disorders, which is closely related to the
70 electrical resistivity (Gomi et al., 2016). Finally we will discuss the implications for
71 alloying hydrogen in the Earth's and planetary cores.

72

METHODS

73 We performed static first-principles calculations of hcp and dhcp iron-hydrogen
74 alloys. The Korringa-Kohn-Rostoker (KKR) method was used as implemented in the
75 AkaiKKR code (Akai, 1989). Perdew-Burke-Ernzerhof (PBE) type of generalized
76 gradient approximation (GGA) was used for the exchange-correlation functional
77 (Perdew et al., 1996). The relativistic effects are taken into account within the scalar
78 relativistic approximation. The wave functions are calculated up to $l = 2$, where l is the
79 angular momentum quantum number. The coherent potential approximation (CPA) was

80 used to represent hydrogen atoms, which randomly occupied the octahedral interstitial
81 site. The hydrogen content x varied from 0.0 (pure iron) to 1.0 (hydrogen saturated iron
82 hydrides) with 0.1 step. The axis ratio is optimized by the total energy minimum at each
83 volume. The number of k -points is set to be at least 312 in the irreducible Brillouin zone.
84 Both spin polarized and non-spin polarized calculations were carried out to represent
85 ferromagnetic and non-magnetic states, respectively. The local moment disorder (LMD)
86 state is also simulated, which is an analog of the paramagnetic state above the Curie
87 temperature (Akai and Dederichs, 1993; see also supplementary text). The energy
88 difference between ferromagnetic and LMD state indicates the relative stability of the
89 ferromagnetism with regards to temperature. Applying the Heisenberg model, the
90 energy difference gives rough value of the Curie temperature, T_C :

$$91 \quad T_C = \frac{2}{3k_B} (E_{\text{LMD}} - E_{\text{ferro}}) \quad (1)$$

92 where k_B is the Boltzmann constant, E_{LMD} and E_{ferro} are total energies of LMD and
93 ferromagnetic states, respectively. This method is used by computational material
94 design of stable magnet for industrial purpose (Sato et al., 2003).

95 RESULTS

96 Fig. 1 shows the total energies of hcp and dhcp, non-magnetic and ferromagnetic
97 FeH_x alloys as a function of volume. In general, non-magnetic phases have smaller V_0
98 than those of ferromagnetic phases. For pure Fe, the most stable phase is non-magnetic
99 hcp Fe with equilibrium volume per formula unit (f.u.) of $V_0 = 70.58 \text{ Bohr}^3/\text{f.u.}$ (10.46
100 $\text{\AA}^3/\text{f.u.}$), followed by ferromagnetic dhcp, non-magnetic dhcp and ferromagnetic hcp Fe
101 at zero pressure. For $\text{FeH}_{1.0}$, the relative stability is in order of ferromagnetic dhcp,

102 ferromagnetic hcp, non-magnetic dhcp and non-magnetic hcp. At higher pressure,
 103 relative phase stability can be obtained by comparison of the enthalpy, $H(V) = E(V) +$
 104 PV . In order to calculate the pressure, we used the 3rd-order isothermal
 105 Birch-Murnaghan equation of states (EoS). First, we fitted the total energy to the $E-V$
 106 relation:

$$107 \quad E(V) = E_0 + \frac{K_0 V}{K'(K'-1)} \left[K' \left(1 - \frac{V_0}{V} \right) + \left(\frac{V_0}{V} \right)^{K'} - 1 \right], \quad (2)$$

108 where E is the total energy, K and K' are the bulk modulus and its pressure derivative,
 109 and V is the volume. Subscript 0 indicates zero pressure value. Supplementary Tables
 110 S1-4 show the fitting parameters. Pressures were then calculated by using the $P-V$
 111 relation:

$$112 \quad P(V) = \frac{3K_0}{2} \left[\left(\frac{V_0}{V} \right)^{\frac{7}{3}} - \left(\frac{V_0}{V} \right)^{\frac{5}{3}} \right] \left\{ 1 + \frac{3}{4} (K'-4) \left[\left(\frac{V_0}{V} \right)^{\frac{2}{3}} - 1 \right] \right\}. \quad (3)$$

113 EoS of ferromagnetic and nonmagnetic dhcp FeH_{1.0} and nonmagnetic hcp Fe are shown
 114 in Fig. 2a. Our calculated results of ferromagnetic dhcp FeH_{1.0} are consistent with
 115 previous results obtained from diamond-anvil cell (DAC) experiments at low pressure
 116 (Hirao et al., 2004; Pépin et al., 2014). However, the calculated volume of
 117 ferromagnetic dhcp FeH_{1.0} deviates at about 30 GPa, and the non-magnetic result
 118 approaches to the experimentally determined volumes at around 60 GPa. This behavior
 119 is consistent with previous calculations (e.g. Elsässer et al. 1998; Tsumuraya et al.,
 120 2012; Pépin et al., 2014). Similarly, our hcp Fe results broadly reproduce the
 121 compression curve of hcp Fe determined by DAC studies (Fei et al, 2016; Dewaele et
 122 al., 2006). Fig. 2b shows the Curie temperature of dhcp FeH_{1.0}, which is comparable to
 123 the Curie temperature of bcc iron at ambient pressure.

124 The same procedure was applied to non-stoichiometric FeH_x alloys calculated by
125 using the CPA. With increasing hydrogen content, V_0 of each phase becomes larger, and
126 hence, ferromagnetic phase tends to become stable (Fig. 1). On the contrary, the
127 pressure effect favors smaller volume phases, which leads to the collapse of
128 ferromagnetism at high pressure. Fig. 2c indicates the most stable crystal/magnetic
129 structure among these four combinations as functions of pressure and hydrogen content.
130 Within the stability field of the ferromagnetic dhcp, the Curie temperature is also shown
131 by broken lines (Fig. 2c).

132 **DISCUSSION**

133 **Magnetic transition pressure**

134 One of the critical discrepancies between first-principles prediction and experimental
135 observation is the magnetic transition pressure. Elsässer et al. (1998) predicted that the
136 stable magnetic structure of FeH is the ferromagnetic, and it transforms to non-magnetic
137 phase at about 60 GPa. This transition pressure is reproduced by subsequent
138 first-principles studies (Pépin et al., 2014; Tsumuraya et al., 2012), further supported by
139 this study (Fig. 2). However, previous DAC experiments implied much lower transition
140 pressure. Mao et al. (2004) conducted nuclear resonant X-ray scattering (NRIXS)
141 experiments up to 52 GPa to obtain compressional velocity and shear wave velocity of
142 FeH. They found the change in slope of these velocity plots above 22 GPa. Shibazaki et
143 al. (2012) performed inelastic X-ray scattering (IXS) measurements up to 70 GPa, and
144 also found similar anomaly at around 30 GPa. Such an anomaly has been interpreted as
145 the magnetic transition from ferromagnetic to non-magnetic state. Indeed, these
146 transition pressures are much lower than theoretical predictions. The local magnetic

147 moments of two Fe sites in dhcp FeH_x have slightly different value, and they are
148 quenched almost simultaneously with compression, which is consistent with previous
149 calculation (Tsumuraya et al., 2012). In addition to the generalized gradient
150 approximation (GGA) for the exchange correlation functional, which likely
151 overestimates the stability field of large volume phases (i.e. ferromagnetic phase), we
152 consider the effect of finite temperature, based on the experimental fact that the Curie
153 transition is second-order phase transition. Previous X-ray diffraction (XRD)
154 measurements (Hirao et al., 2004; Pépin et al., 2014) suggest that the EoS of dhcp FeH
155 is consistent with first-principles EoS of its ferromagnetic phase at pressures below ~30
156 GPa, but the experimental results become gradually deviate from theoretical prediction
157 of ferromagnetic FeH. At pressures above 50 GPa, the experimental data become
158 consistent with theoretical EoS of non-magnetic FeH again. Mitsui and Hirao (2010)
159 conducted *in-situ* Mössbauer measurement up to ~65 GPa. They found rapid
160 disappearance of ferromagnetic 6-line pattern at 27.6 GPa, but there still remains
161 residual weak hyperfine field up to 64.7 GPa. In order to assess the stability of
162 ferromagnetism relative to the paramagnetic state with randomly distributed the
163 momentum directions, we calculated the total energy of the LMD state. The calculated
164 Curie temperature decreases rapidly with applying pressure, and becomes comparable to
165 the ambient temperature at the highest pressure. This behavior is consistent with
166 previous Mössbauer spectroscopy measurements reported by Mitsui and Hirao (2010),
167 as well as XRD study by Hirao et al. (2004). In this study, we only considered the
168 ground state ferromagnetism and the LMD state at the Curie temperature. The
169 contribution to the free energy of intermediate temperature magnetism, as well as finite
170 temperature phonon and fcc phase transition, need to be investigated in the future.

171 Furthermore, it is also important to investigate the sound-wave velocity around the
172 magnetic transition.

173 **Volume of FeH_x alloys**

174 Thermodynamic calculations suggest that the solubility of hydrogen is significantly
175 enhanced at high hydrogen pressure over 3.5 GPa, whereas hydrogen is hardly dissolved
176 into iron at ambient conditions (Sugimoto and Fukai, 1992; Fukai, 1992). This is
177 confirmed from *in-situ* XRD experiments, which show a large volume difference
178 between Fe and FeH_x caused by the occupation of hydrogen atoms into the interstitials
179 (e.g. Hirao et al., 2004; Narygina et al., 2011; Pépin et al., 2014). Against the difficulties
180 arising from the fact that high-pressure polynomials of iron-hydrides cannot be
181 quenched to ambient pressure and temperature, some experiments were conducted to
182 determine the hydrogen or deuterium content at high pressure. Okuchi (1997; 1998)
183 measured the volume fraction of hydrogen bubbles in the iron grains of a recovered
184 sample by means of a rapid-decompression technique. Antonov and co-workers
185 successfully quenched the FeH_x sample to ambient pressure and low temperature by
186 pre-cooling of the sample below 150 K before releasing the pressure, and conducted
187 outgassing (Schneider et al., 1991) and neutron diffraction measurements (Antonov et
188 al., 1998). Recently, Machida et al. (2014) and Iizuka-Oku et al. (2017) reported results
189 from *in-situ* neutron diffraction measurements. However, the maximum pressures of
190 these studies are limited to less than 10 GPa. At higher pressures, *in-situ* XRD
191 measurement is the most common way to determine the volume of FeH_x. In order to
192 estimate the hydrogen content from its volume, the following linear
193 volume-composition relationship is widely used,

$$x = \frac{V_{\text{FeH}_x} - V_{\text{Fe}}}{\Delta V_{\text{H}}} \quad (4)$$

195 where x is hydrogen content, V_{FeH_x} is the volume of FeH_x per formula, V_{Fe} is the atomic
 196 volume of iron, and ΔV_{H} is volume increase per hydrogen atom (see also supplementary
 197 text). The ΔV_{H} has been assumed to be independent of x . This relationship is applicable
 198 to several face-centered cubic (fcc) metal-hydrogen alloys, which is confirmed from
 199 degassing methods (Fig. 3a) (see review in Fukai, 2006). To test the applicability of our
 200 first-principles calculations, we first calculated the equilibrium volume of fcc
 201 metal-hydrogen alloys (PdH_x , NiH_x , $\text{Ni}_{0.8}\text{Fe}_{0.2}\text{H}_x$ and $\text{Fe}_{0.65}\text{Ni}_{0.29}\text{Mn}_{0.06}\text{H}_x$). Our
 202 first-principles results are broadly consistent with previous experimental results (Fukai,
 203 2006), which show nearly linear volume expansion as a function of hydrogen content,
 204 as predicted by Eq. (4) (Fig. 3a). Fig. 3b shows the volume of the most stable phase and
 205 non-magnetic phase of FeH_x as a function of hydrogen content at 20 GPa. Fig 3c
 206 presents the $\Delta V_{\text{H}} = (V_{\text{FeH}_x} - V_{\text{Fe}})/x$. The figures clearly indicate the violation of linearity.
 207 At $x < 0.4$, where the non-magnetic hcp FeH_x phase is stable, the volume increases
 208 almost linearly. However, a discontinuous increase of volume occurs across the phase
 209 transition from non-magnetic hcp to ferromagnetic dhcp phase. Within the
 210 ferromagnetic phase, the volume is almost independent of hydrogen content, suggesting
 211 that the volume of FeH_x phase is mostly controlled by ferromagnetism. Recently,
 212 Iizuka-Oku et al. (2017) reported the result of *in-situ* neutron diffraction measurements
 213 on fcc FeD_x . They compressed Fe with $\text{Mg}(\text{OD})_2$ and SiO_2 mixture as a deuterium
 214 source. The sample was heated to ~ 1000 K at ~ 4 GPa. During the 12 hours holding
 215 time, the Fe sample was progressively deuterated, which is confirmed by the volume
 216 increase and the 111/200 diffraction intensity ratio of fcc FeD_x . The volume expansion

217 exhibited non-linear behavior as a function of the holding time, which might partly be
218 related to the magnetic transition.

219 The volume of ferromagnetic alloys has been interpreted in term of average magnetic
220 moment (see Shiga, 1974 for Review). For example, the lattice constant of Fe-Co
221 system has a maximum at the top of the Slater-Pauling curve. In case of the Fe-H
222 system, the magnetic element is iron only. Therefore, the bulk magnetic moment is
223 almost independent of hydrogen concentration. This is consistent with our
224 first-principles prediction showing little dependence of x on the volume. The Eq. (4) is
225 widely used by many previous studies to estimate the hydrogen content of iron hydride
226 at high pressure (e.g. Yagi and Hishinuma, 1995; Shibazaki et al., 2011; Terasaki et al.,
227 2012; Tagawa et al., 2016). However, our results suggest possible overestimates of the
228 hydrogen content in these experiments because of the assumed linear relationship. Fig.
229 3b also shows that the volume of non-magnetic phase follows the linear relationship
230 predicted by Eq. (4). Such linearity is also observed in non-magnetic phases at higher
231 pressure. Therefore, the Eq. (4) can be applied at pressures higher than ~65 GPa.

232 **Electrical resistivity**

233 It is also worth to mention the effect of magnetism and interstitial hydrogen on the
234 electrical resistivity, since the electrical resistivity, and relevant thermal conductivity, is
235 crucial for the thermal evolution of the Earth (de Koker et al., 2012; Pozzo et al., 2012;
236 Gomi and Hirose, 2015; Gomi et al., 2013; 2016; Seagle et al., 2013; Konôpková et al.,
237 2016; Ohta et al., 2016; Suehiro et al., 2017). The total resistivity of Fe alloys at the
238 core conditions involves many scattering mechanisms, namely phonon scattering,
239 impurity scattering, magnetic scattering and electron-electron correlations. Among them,
240 impurity resistivity of alloying elements is predicted to be predominant and the effect of

241 spin disordered resistivity has been neglected at the Earth's core (see Supplementary Fig.
242 S5 of Gomi et al., 2016). As shown in Gomi et al. (2016), the life time and the mean
243 free path of electrons are relevant to the degree of broadening of the band structure in
244 the vicinity of the Fermi energy via uncertainty relationship. Therefore, we can
245 qualitatively estimate the electrical resistivity from the band structure.

246 Fig. 4a shows the band structure of non-magnetic dhcp Fe. At the stoichiometric
247 composition, the band structure has no broadening because it has no disorder. The
248 broadening increases with increasing hydrogen content, and reaches a maximum at $x =$
249 0.5, which is the highest chemical disorder (Fig. 4c). Above $x = 0.5$, it decreases with
250 recovering the ordering (Fig. 4e). However, it is found that the broadening mainly
251 occurred at far below the Fermi level. This is consistent with the fact that the hydrogen s
252 states locate at around -0.6 Ry from the Fermi energy (Tsumuraya et al., 2012). Even if
253 we considered the electron temperature, the half width at half maximum of the
254 Fermi-Dirac distribution function is 5.58×10^{-2} Ry at $T = 5000$ K (see Supplemental
255 text for detail). Because only electrons at the vicinity of the Fermi energy can contribute
256 the electrical conduction, the effect of disordered hydrogen atoms is predicted to be
257 insignificant to the impurity resistivity.

258 On the other hand, the band structures of LMD state exhibit a strong broadening
259 around the Fermi energy (Fig. 4f-j), which is consistent with the fact that the spin
260 magnetic moment of Fe $4d$ electrons dominates the bulk magnetic moment of FeH_x . As
261 well as the impurity resistivity, this broadening contributes to the electrical resistivity as
262 the spin disordered resistivity (Glasbrenner et al., 2014; Ebert et al., 2015). Considering
263 that both the magnetic moment and the Curie temperature of ferromagnetic hcp and
264 dhcp FeH are comparable to those of bcc Fe, the spin disordered resistivity could be at

265 the same level with that of bcc Fe. This value is comparable to the saturation resistivity,
266 and consistent with previous high P - T resistance measurement of dhcp FeH (Antonov et
267 al., 2002).

268 Previous high pressure and room temperature resistance measurements on dhcp FeH_x
269 showed similar pressure dependence with pure hcp Fe (Matsuoka et al., 2011, Gomi et
270 al., 2013). Assuming that the composition is close to the stoichiometric composition (x
271 = 1.0), dominant scattering mechanism may be lattice vibration. Therefore, the
272 phonon-contributed resistivity of dhcp FeH_x may be comparable to that of hcp Fe.

273 In summary, we considered here three scattering mechanisms on FeH_x alloys at high
274 pressure; impurity resistivity, spin disordered resistivity, and phonon-contributed
275 resistivity. Impurity resistivity of interstitial hydrogen is predicted to be small, whereas
276 that of substitutional silicon is predominant in hcp Fe-Si alloy (Gomi et al., 2013; 2016;
277 Seagle et al., 2013). On the other hand, spin disordered resistivity may have significant
278 contribution within the stable pressure-composition range of ferromagnetic phase at
279 high temperature. Phonon-contributed resistivity of FeH_x may not be significantly
280 different from pure Fe. Thus, we predict that the spin disordered resistivity is
281 predominant at around the Curie temperature and below the magnetic transition pressure,
282 and it will largely decrease in conjunction with the disappearance of its magnetism.

283

IMPLICATIONS

284 The calculations indicate that ferromagnetism in FeH_x collapses above ~65 GPa,
285 accompanied with significant changes in physical properties. One of the important
286 findings of this study is the absence of strong scattering mechanism in FeH_x alloys at the
287 Earth's core conditions. Gomi et al. (2016) found that the Si impurity resistivity is

288 predominant in Fe-Ni-Si ternary alloy at the core P - T conditions (see Supplementary
 289 Fig. S5 of Gomi et al., 2016). However, we predict that H impurity should not
 290 contribute to the electron scattering (Fig. 4 a-e). Another possible scattering mechanism
 291 is magnetic disorder (Drchal et al., 2017). Although it indeed exhibits strong broadening
 292 of the band structure (Fig.4 f-j), the ferromagnetic state becomes unstable above ~ 60
 293 GPa, leading to no contribution to resistivity of the Earth's core. Therefore, if hydrogen
 294 were the predominant alloying light elements in the Earth's core, the total core
 295 resistivity would be smaller than our previous estimates based on Fe-Ni-Si ternary core
 296 model (Gomi et al., 2016).

297 In order to understand the thermal evolution of hydrogen-bearing Earth's core, we
 298 develop an $\text{Fe}_{1-y}\text{Si}_y\text{H}_x$ ternary composition model for the Earth's outer core as follows.
 299 First, we modeled the outer core temperature as function of hydrogen content, x . The
 300 melting temperature of pure Fe at the inner core boundary (ICB) pressure is
 301 extrapolated to be ~ 6200 K (Anzellini et al., 2013; Alfè, 2009), and that of $\text{FeH}_{1.0}$ is
 302 ~ 3500 K (Sakamaki et al., 2009). Note that Si may not significantly decrease the
 303 melting temperature (Fischer et al., 2013). Assuming that the melting temperature
 304 reduction is proportional to x , the present-day ICB temperature may be $T_{\text{ICB}p}(x) = 6200$
 305 $- 2700x$ K. The CMB temperature can be estimated from the adiabatic temperature
 306 gradient, $T_{\text{CMB}p}(x) = T_{\text{ICB}p}(x) \left(\rho_{\text{CMB}}^{\text{density}} / \rho_{\text{ICB}}^{\text{density}} \right)^\gamma$, where $\gamma = 1.5$ is the Grüneisen parameter
 307 (Vočadlo et al., 2003), $\rho_{\text{CMB}}^{\text{density}} = 9.90349 \text{ g/cm}^3$ and $\rho_{\text{ICB}}^{\text{density}} = 12.16634 \text{ g/cm}^3$ are
 308 densities at the CMB and the ICB, respectively (Dziewonsk and Anderson, 1981). The
 309 present-day CMB temperature is plotted in Fig. 6 (a).

310 Next, we calculated the Si content, y , based on the comparison between the PREM
311 density and that calculated from the EoS of $\text{Fe}_{1-y}\text{Si}_y\text{H}_x$ alloy at the CMB pressure and
312 temperature (Fig. 5). Assuming that the volume increase $x\Delta V_{\text{H}}$ depends only on pressure,
313 and independent of temperature and Si content, we formulated the EoS of $\text{Fe}_{1-y}\text{Si}_y\text{H}_x$
314 alloy to be $P_{\text{Fe-Si-H}}(V, T, x, y) = P_{\text{Fe-Si}}(V - x\Delta V_{\text{H}}, T, y)$. Following Tateno et al. (2015), the
315 EoS of $\text{Fe}_{1-y}\text{Si}_y$ alloy is obtained by linear interpolation between the EoS of hcp Fe
316 (Dewaele et al., 2006) and that of hcp Fe + 9wt.% Si alloy (Tateno et al., 2015). The
317 $x\Delta V_{\text{H}}$ is calculated from EoS of hcp FeH_x of this study. Fig 6 (b) represents the Si
318 content as a function of the H content. The Si content decreases with increasing the H
319 content, as expected. Because of the convection, the composition is uniform throughout
320 the outer core. The calculated density profiles of all compositions considered here are
321 broadly consistent with the PREM at deep portion of the outer core (Fig. 5).

322 Then, we modeled the thermal conductivity of the ternary alloy. Similar to the model
323 used by Gomi et al. (2016), we adopted the following core resistivity model with the
324 resistivity saturation, which is proposed by Cote and Meisel (1978)

$$325 \quad \rho_{\text{tot}}(V, T) = \left(1 - \frac{\rho_{\text{tot}}(V, T)}{\rho_{\text{sat}}(V)}\right) \rho_{\text{ph,ideal}}(V, T) + \rho_{\text{imp}}(V, y) \exp(-2W(V, T)) \quad (5)$$

326 where $\rho_{\text{tot}}(V, T)$ is the total resistivity, $\rho_{\text{sat}}(V)$ is the saturation resistivity, $\rho_{\text{ph,ideal}}(V, T)$ is
327 the “ideal” phonon-contributed resistivity which neglects the effect of the resistivity
328 saturation, $\rho_{\text{imp}}(V, y)$ is the impurity resistivity at zero Kelvin, and $\exp(-2W(T))$ is the
329 Debye-Waller factor which gives temperature coefficient of impurity resistivity. We
330 must emphasize the absence of the magnetic scattering term in Eq (5). For the
331 ferromagnetic body-centered cubic (bcc) Fe, the magnetic scattering resistivity is about
332 double of the phonon contributed resistivity at 1 bar and at the Curie temperature

333 (Bäcklund, 1961). The experimentally measured total resistivity of ferromagnetic dhcp
334 FeH at ~6 GPa (Antonov et al., 1982; 2002) shows a high resistance. The resistance
335 ratio is $R/R_0 \sim 9$ at 330 °C, where the subscript 0 indicates the ambient conditions.
336 Assuming $\rho = \rho_0 R/R_0$ and $\rho_0 = 1.0 \times 10^{-7} \Omega\text{m}$, the estimated resistivity is $\sim 9 \times 10^{-7} \Omega\text{m}$,
337 which is comparable to that of bcc Fe. The present calculations on the band structure of
338 the LMD dhcp FeH_x show strong broadenings (Fig. 4), which imply a large magnetic
339 scattering resistivity, consistent with the results of Antonov et al. (1982; 2002). If such
340 magnetic moments are not quenched at the Earth's core condition, the magnetic
341 scattering resistivity should have a large contribution to the total resistivity. However,
342 our total energy calculations indicate that the stability field of ferromagnetic FeH_x is
343 limited below ~ 65 GPa, suggesting the absence of magnetic scattering at the Earth's
344 core, whose pressure range is above 135 GPa. We also neglected the effect of
345 electron-electron correlations, which may not be significant (Pourovskii et al., 2014).
346 The saturation resistivity is assumed to be proportional to $V^{1/3}$ (Gomi et al., 2013)

$$347 \quad \rho_{\text{sat}}(V) = \rho_{\text{sat}}(V_0) \left(\frac{V}{V_0} \right)^{\frac{1}{3}} \quad (6)$$

348 where $\rho_{\text{sat}}(V_0) = 1.68 \times 10^{-6} \Omega\text{m}$ is the saturation resistivity at 1 bar obtained from
349 resistivity measurements on bcc and fcc Fe-based alloys (Bohnenkamp et al., 2002). We
350 assumed that the phonon-contributed resistivity of dhcp FeH_x is very close to that of hcp
351 Fe, which can be extrapolated from 300 K measurements of hcp Fe reported by Gomi et
352 al. (2013). At around 300 K, the resistivity can be calculated by using the
353 Bloch-Grüneisen formula,

$$354 \quad \rho_{\text{ph,ideal}}(V, T) = B(V) \left(\frac{T}{\Theta_D(V)} \right)^5 \int_0^{\Theta_D(V)/T} \frac{z^5 dz}{(\exp(z) - 1)(1 - \exp(-z))} \quad (7)$$

355 where $B(V)$ is the material constant (Gomi et al., 2013) and $\Theta_D(V)$ is the Grüneisen
 356 parameter (Dewaele et al., 2006). The Bloch-Grüneisen formula can reproduce the
 357 temperature dependence of hcp Fe up to 450 K (Gomi et al., 2013; Ohta et al., 2016).
 358 However, it will be violated because of the resistivity saturation, and the total resistivity
 359 of pure metals can reasonably be represented by the Shub-nikovich model (Wiesmann et
 360 al. 1977).

$$361 \quad \frac{1}{\rho_{\text{tot}}(V,T)} = \frac{1}{\rho_{\text{ph,ideal}}(V,T)} + \frac{1}{\rho_{\text{sat}}(V)} \quad (8)$$

362 Note that, if we ignore the impurity resistivity, Eq (5) is equivalent to the Shub-nikovich
 363 model (Eq 8).

364 It is still being discussed the amount and the composition of light alloying elements
 365 in the Earth's Fe-Ni dominant core. The presence of the impurity elements causes an
 366 additional scattering of electron in metal, which is the origin of impurity resistivity. For
 367 the impurity resistivity in the core, the effect of alloying Si has been most widely
 368 investigated (Mattasov, 1977; Stacey and Anderson, 2001; Seagle et al., 2013; Gomi et
 369 al., 2013; 2016; Kiarasi and Secco, 2015). Gomi et al. (2016) suggested that the Si
 370 impurity resistivity is larger than the phonon-contributed resistivity and the Ni impurity
 371 resistivity for the hypothetical Fe-Ni-Si composition. This inversely implies that, if the
 372 actual light elements have smaller impurity resistivity than Si impurity, the estimated
 373 total resistivity should largely be decreased. In this study, it is found that almost no
 374 broadening of the band structure in the vicinity of the Fermi energy due to the H
 375 disorder effect, which qualitatively indicates no H impurity resistivity. Therefore, we
 376 assumed that the impurity resistivity depends only on the Si content. The CMB value is
 377 interpolated from the first-principles results at $V = 16.27 \text{ \AA}^3$ reported by Gomi et al.
 378 (2016). Assuming the Debye model, $W(T)$ can be obtained as follows (Markowitz,

379 1976)

$$380 \quad W(T) = \frac{3\eta^2 K^2 T^2}{2mk_B \Theta_D^3} \int_0^{\Theta_D/T} \left(\frac{1}{\exp(z) - 1} + \frac{1}{2} \right) z dz \quad (9)$$

381 where \hbar is the reduced Planck's constant (the Dirac's constant), k_B is the Boltzmann
382 constant, m is the atomic mass, and K is electronic wave vector transfer. Although it
383 decreases the impurity resistivity with increasing temperature, the Debye-Waller factor
384 $\exp(-2W(T))$ is very close to unity in general (Rossiter, 1978; Markowitz, 1976) and can
385 be negligible even at the Earth's core temperature condition (Gomi et al., 2016). Usually,
386 the resistivity of metals increases upon melting, however, its magnitude is basically
387 small for transition metals (Faber, 1972). The resistivity enhancement is $\sim 8\%$ for Fe at
388 1 bar (Van Zytveld, 1980) and 7 GPa (Secco and Schloessin, 1989). Recently, Wagle
389 and Steinle-Neumann (2018) suggested that the resistivity change decreases with
390 pressure and to be negligibly small at the inner core boundary. This situation is also
391 valid for the thermal conductivity (Nishi et al., 2003). Therefore, we simply ignored this
392 effect. The thermal conductivity was then estimated from the Wiedemann-Franz law,
393 $k = LT / \rho_{\text{tot}}$ where k is the thermal conductivity, and L is the Lorenz number. Applying
394 the Sommerfeld expansion, the Lorenz number is estimated to $L_{\text{Sommer}} = 2.45 \times 10^{-8}$
395 $\text{W}\Omega\text{K}^{-2}$ (Gomi and Hirose, 2015). This could be potentially violated, which yields about
396 40 % of the maximum uncertainty (Gomi and Hirose, 2015; Secco, 2017). However, we
397 used the Sommerfeld value of the Lorenz number as a representative value. Fig 6 (c)
398 shows the present-day conductivity at the top of the outer core. The effect of H alloying
399 causes the reduction of melting temperature and electrical resistivity. These two factors,
400 which have opposite contribution to the thermal conductivity, are almost cancelled out.
401 Therefore, the thermal conductivity is $\sim 100 \text{ W/m/K}$, which is almost constant versus H

402 content. The estimated thermal conductivity is comparable to the high values obtained
403 from recent theoretical and experimental studies (Pozzo et al., 2012; de Koker et al.,
404 2012; Ohta et al., 2016; Gomi and Hirose, 2015; Gomi et al., 2013; 2016).

405 Finally, we solved the energy conservation equations of the core to calculate the
406 thermal history of the Earth's core (Labrosse, 2015; Gomi et al., 2013, 2016; see also
407 Supplementary text). We assumed that the CMB heat flow is always equal to the
408 isentropic heat flow at the CMB, which maximize the inner core age. We did not
409 consider any contribution from radioactive elements. The calculated maximum inner
410 core age is 0.49 Gyr at $x = 0$, whereas it increases to 0.86 Gyr at $x = 0.7$ (Fig 6 d). This
411 is because the incorporation of hydrogen contributes to the reduction of the core
412 temperature, which decreases the core adiabatic temperature gradient (Gomi and Hirose,
413 2015). Previous estimates of the inner core age are highly uncertain. The high value of
414 thermal conductivity (c.a. ~ 100 W/m/K) indicates young inner core (< 1 Gyr) (e.g.
415 Gomi et al., 2013; 2016; Gomi and Hirose, 2015; Ohta et al., 2016; Pozzo et al. 2012;
416 de Koker et al., 2012), whereas the low value (c.a. ~ 30 W/m/K) allows much older
417 inner core (~ 3 Gyr) (Stacey and Loper, 2007; Konopkova et al., 2016). Even though the
418 effects of hydrogen increase the maximum inner core age, our new value of young inner
419 core age is inconsistent with the Mesoproterozoic (~ 1.3 Ga) inner core nucleation
420 proposed by Bigin et al. (2015). Reconciliation of the difference requires further
421 examination of the palaeomagnetic intensity data (Smirnov et al., 2016) and assessment
422 of energy budget in early history of the Earth.

423 The effect of ferromagnetism may play an important role in smaller planets and
424 satellites, if their iron-dominant cores contain hydrogen. For example, such a situation
425 likely occurs at the interior of the Ganymede, which contains large amount of hydrogen

426 as the thick icy mantle, and hence, coexisting iron may react to form iron hydrides
427 (Fukai, 1984; Okuchi, 1997; Yagi and Hishinuma 1995; Shibazaki et al., 2011; Terasaki
428 et al., 2012). Our prediction of the Curie temperature of dhcp $\text{FeH}_{1.0}$ is comparable to
429 the temperature of interior of these smaller bodies (e.g. Kimura et al., 2009). If the
430 internal temperature is below the Curie temperature, the FeH_x alloy has spontaneous
431 magnetism and could be a source of remnant magnetism of the bodies (e.g. Crary and
432 Bagenal, 1998). Note that the electron band structure of LMD state is significantly
433 different from that of non-magnetic phase, which also emphasizes the importance of
434 ferromagnetism, even if the internal temperature is above the Curie temperature.

435

ACKNOWLEDGMENTS

436 Postdoctoral fellowship to H.G. is supported by the NASA (NNX14AG26G) and NSF
437 (EAR-1214990) grants to Y.F. This work was also supported by JSPS
438 MEXT/KAKENHI Grant Number JP15H05827. We thank two anonymous reviewers
439 for their constructive comments and suggestions.

440

REFERENCES CITED

441

442 Akai, H. (1989) Fast Korringa-Kohn-Rostoker coherent potential approximation and its
443 application to FCC Ni-Fe systems, *Journal of Physics: Condensed Matter*, 1(43),
444 8045-8063.

445 Akai, H., and Dederichs, P. H. (1993) Local moment disorder in ferromagnetic alloys,
446 *Physical Review B*, 47(14), 8739-8747.

447 Alfè, D. (2009). Temperature of the inner-core boundary of the Earth: Melting of iron at
448 high pressure from first-principles coexistence simulations. *Physical Review B*,
449 79(6), 060101.

450 Antonov, V. E., Belash, I. T., and Ponyatovsky, E. G. (1982). T-P phase diagram of the
451 Fe-H system at temperatures to 450 °C and pressures to 6.7 GPa. *Scripta*
452 *Metallurgica*, 16(2), 203-208. Antonov, V. E., Cornell, K., Fedotov, V. K.,
453 Kolesnikov, A. I., Ponyatovsky, E. G., Shiryayev, V. I., and Wipf, H. (1998) Neutron
454 diffraction investigation of the dhcp and hcp iron hydrides and deuterides. *Journal*
455 *of Alloys and Compounds*, 264(1), 214-222.

456 Antonov, V., Baier, M., Dorner, B., Fedotov, V., Grosse, G., Kolesnikov, A.,
457 Ponyatovsky, E., Schneider, G., and Wagner, F. (2002) High-pressure hydrides of
458 iron and its alloys, *Journal of Physics: Condensed Matter*, 14(25), 6427-6445.

459 Anzellini, S., Dewaele, A., Mezouar, M., Loubeyre, P., and Morard, G. (2013). Melting
460 of iron at Earth's inner core boundary based on fast X-ray diffraction. *Science*,
461 340(6131), 464-466.

462 Biggin, A. J., Piispa, E. J., Pesonen, L. J., Holme, R., Paterson, G. A., Veikkolainen, T.,
463 and Tauxe, L. (2015) Palaeomagnetic field intensity variations suggest
464 Mesoproterozoic inner-core nucleation. *Nature*, 526(7572), 245-248.

465 Birch, F. (1964) Density and composition of mantle and core, *Journal of Geophysical*
466 *Research*, 69(20), 4377-4388.

467 Bohnenkamp, U., Sandström, R., and Grimvall, G. (2002). Electrical resistivity of steels
468 and face-centered-cubic iron. *Journal of Applied Physics*, 92(8), 4402-4407.

469 Caracas, R. (2015) The influence of hydrogen on the seismic properties of solid iron,
470 *Geophysical Research Letters*, 42(10), 3780-3785.

471 Crary, F. J., and Bagenal, F. (1998) Remanent ferromagnetism and the interior structure
472 of Ganymede, *Journal of Geophysical Research*, 103(E11), 25757-25773.

473 Cote, P. J., and Meisel, L. V. (1978). Origin of saturation effects in electron transport.
474 *Physical Review Letters*, 40(24), 1586-1589.

475 de Koker, N., Steinle-Neumann, G., and Vlček, V. (2012) Electrical resistivity and
476 thermal conductivity of liquid Fe alloys at high P and T, and heat flux in Earth's
477 core. *Proceedings of the National Academy of Sciences of the United States of*
478 *America*, 109(11), 4070-4073.

479 Dewaele, A., Loubeyre, P., Occelli, F., Mezouar, M., Dorogokupets, P. I., and Torrent,
480 M., (2006) Quasihydrostatic equation of state of iron above 2 Mbar, *Physical*
481 *Review Letters*, 97(21), 215504.

482 Drchal, V., Kudrnovský, J., Wagenknecht, D., Turek, I., and Khmelevskyi, S. (2017).
483 Transport properties of iron at Earth's core conditions: The effect of spin disorder.
484 *Physical Review B*, 96(2), 024432.

485 Dziewonski, A. M., and Anderson, D. L. (1981). Preliminary reference Earth model.
486 *Physics of the Earth and Planetary Interiors*, 25(4), 297-356.

487 Ebert, H., Mankovsky, S., Chadova, K., Polesya, S., Minár, J., and Ködderitzsch, D.
488 (2015) Calculating linear-response functions for finite temperatures on the basis of

489 the alloy analogy model, *Physical Review B*, 91(16), 165132.

490 Elsässer, C., Zhu, J., Louie, S., Meyer, B., and Chan, C. (1998) Ab initio study of iron
491 and iron hydride: II. Structural and magnetic properties of close-packed Fe and
492 FeH, *Journal of Physics: Condensed Matter*, 10(23), 5113-5129.

493 Faber, T. E. (1972) *Introduction to the Theory of Liquid Metals*. Cambridge at the
494 University Press.

495 Fei, Y. Murphy, C., Shibazaki, Y., Shahar, and A. Huang, H. (2016) Thermal equation of
496 state of hcp-iron: Constraint on the density deficit of Earth's solid inner core,
497 *Geophysical Research Letters*, 43(13), 6837-6843.

498 Fischer, R. A., Campbell, A. J., Reaman, D. M., Miller, N. A., Heinz, D. L., Dera, P.,
499 and Prakapenka, V. B. (2013). Phase relations in the Fe–FeSi system at high
500 pressures and temperatures. *Earth and Planetary Science Letters*, 373, 54-64.

501 Fukai, Y. (1984) The iron-water reaction and the evolution of the Earth, *Nature* 308,
502 174-175.

503 Fukai, Y. (1992) Some properties of the Fe–H system at high pressures and temperatures,
504 and their implications for the Earth's core, *High-pressure Research: Application to*
505 *Earth and Planetary Science*, 373-385.

506 Fukai, Y. (2006) *The metal-hydrogen system: basic bulk properties*, Springer Science &
507 Business Media.

508 Glasbrenner, J. K., Pujari, B. S., and Belashchenko, K. D. (2014) Deviation from
509 Matthiessen's rule and resistivity saturation effects in Gd and Fe from first
510 principles, *Physical Review B*, 89(16), 174498.

511 Gomi, H., and Hirose, K. (2015) Electrical resistivity and thermal conductivity of hcp
512 Fe–Ni alloys under high pressure: Implications for thermal convection in the

513 Earth's core, *Physics of the Earth and Planetary Interior*, 247, 2-10.

514 Gomi, H., Hirose, K., Akai, H., and Fei, Y. (2016) Electrical resistivity of
515 substitutionally disordered hcp Fe–Si and Fe–Ni alloys: Chemically-induced
516 resistivity saturation in the Earth's core, *Earth and Planetary Science Letters*, 451,
517 51-61.

518 Gomi, H., Ohta, K., Hirose, K., Labrosse, S., Caracas, R., Verstraete, M. J., and
519 Hernlund, J. W. (2013) The high conductivity of iron and thermal evolution of the
520 Earth's core, *Physics of Earth and Planetary Interior*, 224, 88-103.

521 Hirao, N., Kondo, T., Ohtani, E., Takemura, K., and Kikegawa, T. (2004) Compression
522 of iron hydride to 80 GPa and hydrogen in the Earth's inner core, *Geophysical
523 Research Letters*, 31(6), L06616.

524 Iizuka-Oku, R., Yagi, T., Gotou, H., Okuchi, T., Hattori, T., and Sano-Furukawa, A.
525 (2017) Hydrogenation of iron in the early stage of Earth's evolution. *Nature
526 communications*, 8, 14096.

527 Isaev, E. I., Skorodumova, N. V., Ahuja, R., Vekilov, Y. K., and Johansson, B. (2007)
528 Dynamical stability of Fe-H in the Earth's mantle and core regions, *Proceedings of
529 the National Academy of Sciences of the United States of America*, 104(22),
530 9168-9171.

531 Kiarasi, S., and Secco, R. A. (2015). Pressure - induced electrical resistivity saturation
532 of Fe₁₇Si. *physica status solidi (b)*, 252(9), 2034-2042.

533 Kimura, J., Nakagawa, T., and Kurita, K. (2009) Size and compositional constraints of
534 Ganymede's metallic core for driving an active dynamo. *Icarus*, 202(1), 216-224.

535 Konôpková, Z., McWilliams, R. S., Gómez-Pérez, N., and Goncharov, A. F. (2016)
536 Direct measurement of thermal conductivity in solid iron at planetary core

537 conditions, *Nature*, 534(7605), 99-101.

538 Labrosse, S. (2015) Thermal evolution of the core with a high thermal
539 conductivity. *Physics of the Earth and Planetary Interior*, 247, 36-55.

540 Machida, A., Saitoh, H., Sugimoto, H., Hattori, T., Sano-Furukawa, A., Endo, N.,
541 Katayama, Y., Iizuka, R., Sato, T., Matsuo, M., Orimo, S., and Aoki, K. (2014) Site
542 occupancy of interstitial deuterium atoms in face-centred cubic iron, *Nature*
543 *communications.*, 5, 5063.

544 Mao, W. L., Sturhahn, W., Heinz, D. L., Mao, H. K., Shu, J., and Hemley, R. J. (2004)
545 Nuclear resonant x-ray scattering of iron hydride at high pressure, *Geophysical*
546 *Research Letters*, 31(15), L15618.

547 Markowitz, D., (1977). Calculation of electrical resistivity of highly resistive metallic
548 alloys. *Physical Review B* 15, 3617-3619.

549 Matassov, G., (1977), The electrical conductivity of iron-silicon alloys at high pressures
550 and the Earth's core. PhD thesis, Lawrence Livermore Lab., Univ. California.

551 Matsuoka, T., Hirao, N., Ohishi, Y., Shimizu, K., Machida, A., and Aoki, K. (2011)
552 Structural and electrical transport properties of FeH_x under high pressures and low
553 temperatures, *High Pressure Research*, 31(1), 64-67.

554 Mitsui, T., and Hirao, N. (2010) Ultrahigh-pressure study on the magnetic state of iron
555 hydride using an energy domain synchrotron radiation ⁵⁷Fe Mössbauer
556 spectrometer, *Materials Research Society Symposium Online Proceedings Library*,
557 1262, 115-119.

558 Narygina, O., Dubrovinsky, L. S., McCammon, C. A., Kurnosov, A., Kantor, I. Y.,
559 Prakapenka, V. B., and Dubrovinskaia, N. A. (2011) X-ray diffraction and
560 Mössbauer spectroscopy study of fcc iron hydride FeH at high pressures and

561 implications for the composition of the Earth's core, *Earth and Planetary Science*
562 *Letters*, 307(3), 409-414.

563 Nishi, T., Shibata, H., Ohta, H., and Waseda, Y. (2003) Thermal conductivities of molten
564 iron, cobalt, and nickel by laser flash method. *Metallurgical and Materials*
565 *Transactions A*, 34, 2801-2807.

566 Ohta, K., Kuwayama, Y., Hirose, K., Shimizu, K., and Ohishi, Y. (2016) Experimental
567 determination of the electrical resistivity of iron at Earth's core conditions. *Nature*,
568 534(7605), 95-98.

569 Okuchi, T. (1997) Hydrogen partitioning into molten iron at high pressure: implications
570 for Earth's core. *Science*, 278(5344), 1781-1784.

571 Okuchi, T., (1998). The melting temperature of iron hydride at high pressures and its
572 implications for the temperature of the Earth's core, *Journal of Physics: Condensed*
573 *Matter*, 10(49), 11595-11598.

574 Pépin, C. M., Dewaele, A., Geneste, G., Loubeyre, P., and Mezouar, M. (2014) New
575 iron hydrides under high pressure, *Physical Review Letters*, 113(26), 265504.

576 Perdew, J. P., Burke, K., and Ernzerhof, M. (1996) Generalized gradient approximation
577 made simple, *Physical Review Letters*, 77(18), 3865-3868.

578 Pourovskii, L. V., Mravlje, J., Ferrero, M., Parcollet, O., and Abrikosov, I. A. 2014.
579 Impact of electronic correlations on the equation of state and transport in ϵ -Fe.
580 *Physical Review B*, 90(15), 155120.

581 Pozzo, M., Davies, C., Gubbins, D., and Alfe, D. (2012) Thermal and electrical
582 conductivity of iron at Earth's core conditions. *Nature*, 485(7398), 355-358.

583 Rossiter, P.L., 1987. *The electrical resistivity of metals and alloys*. Cambridge
584 University Press.

585 Sakamaki, K., Takahashi, E., Nakajima, Y., Nishihara, Y., Funakoshi, K., Suzuki, T., and
586 Fukai, Y., (2009) Melting phase relation of FeH_x up to 20GPa: Implication for the
587 temperature of the Earth's core, *Physics of the Earth and Planetary Interior*, 174(1),
588 192-201.

589 Sato, K., Dederics, P., and Katayama-Yoshida, H., (2003) Curie temperatures of III–V
590 diluted magnetic semiconductors calculated from first principles, *Europhysics*
591 *Letters*, 61(3), 403-408.

592 Schneider, G., Baier, M., Wordel, R., Wagner, F. E., Antonov, V. E., Ponyatovsky, E. G.,
593 Kopilovskii, Y., and Makarov, E. (1991) Mössbauer study of hydrides and
594 deuterides of iron and cobalt. *Journal of the Less Common Metals*, 172,
595 333-342.

596 Seagle, C. T., Cottrell, E., Fei, Y., Hummer, D. R., and Prakapenka, V. B. (2013)
597 Electrical and thermal transport properties of iron and iron–silicon alloy at high
598 pressure. *Geophysical Research Letters*, 40(20), 5377-5381.

599 Secco, R. A. 2017. Thermal conductivity and Seebeck coefficient of Fe and Fe-Si
600 alloys: Implications for variable Lorenz number. *Physics of Earth and Planetary*
601 *Interior*, 265, 23-34.

602 Secco, R.A., Schloessin, H.H., 1989. The electrical resistivity of solid and liquid Fe at
603 pressure up to 7 GPa. *Journal of Geophysical Research* 94, 5887-5894.

604 Shibazaki, Y., Ohtani, E., Fukui, H., Sakai, T., Kamada, S., Ishikawa, D., Tsutsui, S.,
605 Baron, A. Q., Nishitani, N., and Hirao, N. (2012) Sound velocity measurements in
606 dhcp-FeH up to 70GPa with inelastic X-ray scattering: Implications for the
607 composition of the Earth's core, *Earth and Planetary Science Letters*, 313, 79-85.

608 Shibazaki, Y., Ohtani, E., Terasaki, H., Tateyama, R., Sakamaki, T., Tsuchiya, T., and

609 Funakoshi, K. I. (2011) Effect of hydrogen on the melting temperature of FeS at
610 high pressure: Implications for the core of Ganymede, Earth and Planetary Science
611 Letters, 301(1-2). 153-158

612 Shibazaki, Y., Terasaki, H., Ohtani, E., Tateyama, R., Nishida, K., Funakoshi, K., and
613 Higo, Y., (2014) High-pressure and high-temperature phase diagram for
614 $\text{Fe}_{0.9}\text{Ni}_{0.1}\text{-H}$ alloy, Physics of the Earth and Planetary Interior 228, 192-201.

615 Shiga, M. (1974) Correlation between lattice constant and magnetic moment in 3d
616 transition metal alloys, AIP Conference Proceedings, 18(1), 463-477.

617 Smirnov, A. V., Tarduno, J. A., Kulakov, E. V., McEnroe, S. A., and Bono, R. K. (2016)
618 Palaeointensity, core thermal conductivity and the unknown age of the inner core.
619 Geophysical Journal International, 205(2), 1190-1195.

620 Stacey, F. D., and Anderson, O. L. (2001). Electrical and thermal conductivities of Fe–
621 Ni–Si alloy under core conditions. Physics of the Earth and Planetary Interiors,
622 124(3-4), 153-162.

623 Stacey, F. D., and Loper, D. E. (2007). A revised estimate of the conductivity of iron
624 alloy at high pressure and implications for the core energy balance. Physics of the
625 Earth and Planetary Interiors, 161(1-2), 13-18.

626 Suehiro, S., Ohta, K., Hirose, K., Morard, G., and Ohishi, Y. (2017) The influence of
627 sulfur on the electrical resistivity of hcp iron: Implications for the core conductivity
628 of Mars and Earth. Geophysical Research Letters, 44,

629 Sugimoto, H., and Fukai, Y. (1992) Solubility of hydrogen in metals under high
630 hydrogen pressures: thermodynamical calculations. Acta Metallurgica et Materialia,
631 40(9), 2327-2336.

632 Tagawa, S., Ohta, K., Hirose, K., Kato, C., and Ohishi, Y. (2016) Compression of Fe–

633 Si–H alloys to core pressures, *Geophysical Research Letters*, 43(8), 3686-3692.

634 Tateno, S., Kuwayama, Y., Hirose, K., and Ohishi, Y. (2015). The structure of Fe–Si
635 alloy in Earth's inner core. *Earth and Planetary Science Letters*, 418, 11-19.

636 Terasaki, H., Ohtani, E., Sakai, T., Kamada, S., Asanuma, H., Shibazaki, Y., Hirao, N.,
637 Sata, N., Ohishi, Y., Sakamaki, T., Suzuki, A., and Funakoshi, K. (2012) Stability
638 of Fe–Ni hydride after the reaction between Fe–Ni alloy and hydrous phase
639 (δ -AlOOH) up to 1.2 Mbar: Possibility of H contribution to the core density deficit.
640 *Physics of the Earth and Planetary Interior*, 194-195, 18-24.

641 Tsumuraya, T., Matsuura, Y., Shishidou, T., and Oguchi, T. (2012) First-principles study
642 on the structural and magnetic properties of iron hydride, *Journal of Physical
643 Society of Japan.*, 81(6), 064707.

644 Umemoto, K., and Hirose, K. (2015) Liquid iron-hydrogen alloys at outer core
645 conditions by first-principles calculations, *Geophysical Research Letters*, 42(18),
646 7513-7520.

647 Van Zytveld, J. B. (1980). Electrical resistivities of liquid transition metals. *Le Journal
648 de Physique Colloques*, 41(C8), C8-503.

649 Vočadlo, L., Alfe, D., Gillan, M. J., and Price, G. D. (2003). The properties of iron
650 under core conditions from first principles calculations. *Physics of the Earth and
651 Planetary Interiors*, 140(1-3), 101-125.

652 Wagle, F., and Steinle-Neumann, G. (2018) Electrical resistivity discontinuity of iron
653 along the melting curve. *Geophysical Journal International*, 213, 237-243.

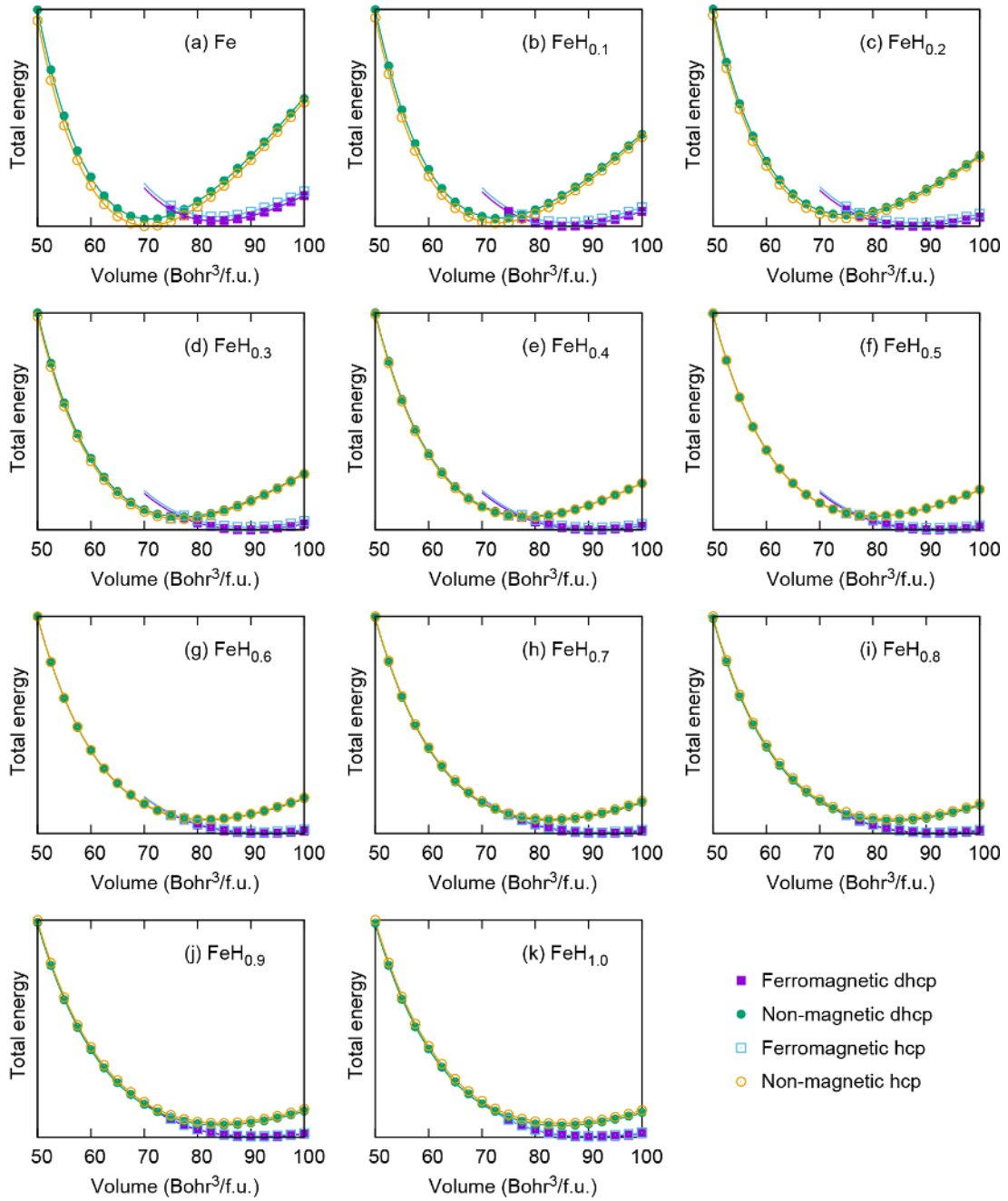
654 Wiesmann, H., Gurvitch, M., Lutz, H., Gohsh, A., Schwarz, B., Strongin, M., Allen, P.B.,
655 and Halley, J.W. 1977. Simple model for characterizing the electrical resistivity in
656 A-15 superconductors. *Physical Review. Letters*. 38, 782-785.

657 Yagi, T., and Hishinuma, T. (1995). Iron hydride formed by the reaction of iron, silicate,
658 and water: Implications for the light element of the Earth's core. *Geophysical*
659 *Research Letters*, 22(14), 1933-1936.

660 Yamakata, M., Yagi, T., Utsumi, W., and Fukai, Y. (1992) In situ X-ray observation of
661 iron hydride under high pressure and high temperature, *Proceedings of the Japan*
662 *Academy, Series B*, 68(10), 172-176.

663

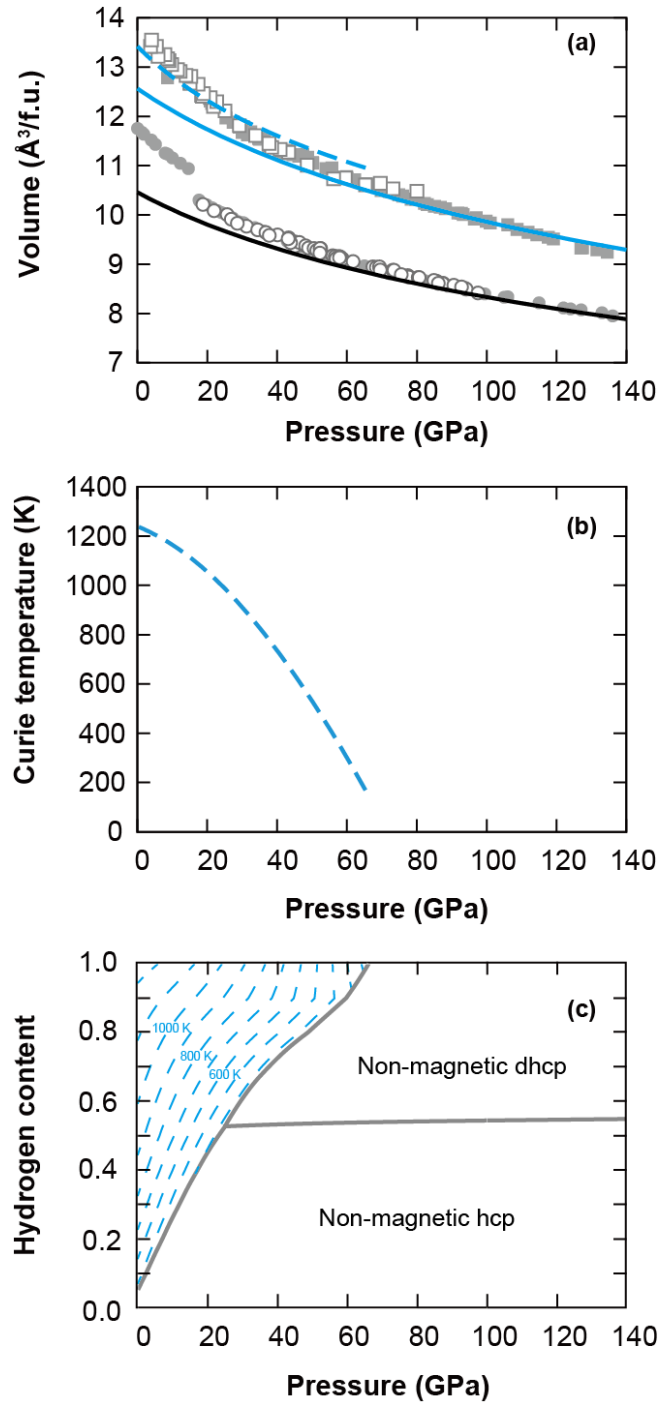
664



665

666 **Fig. 1.** Total energy of hcp and dhcp FeH_x with ferromagnetic and non-magnetic spin
 667 alignment, where x is hydrogen content (filled square: ferromagnetic dhcp, filled circle:
 668 non-magnetic dhcp, open square: ferromagnetic hcp, open circle: non-magnetic hcp).

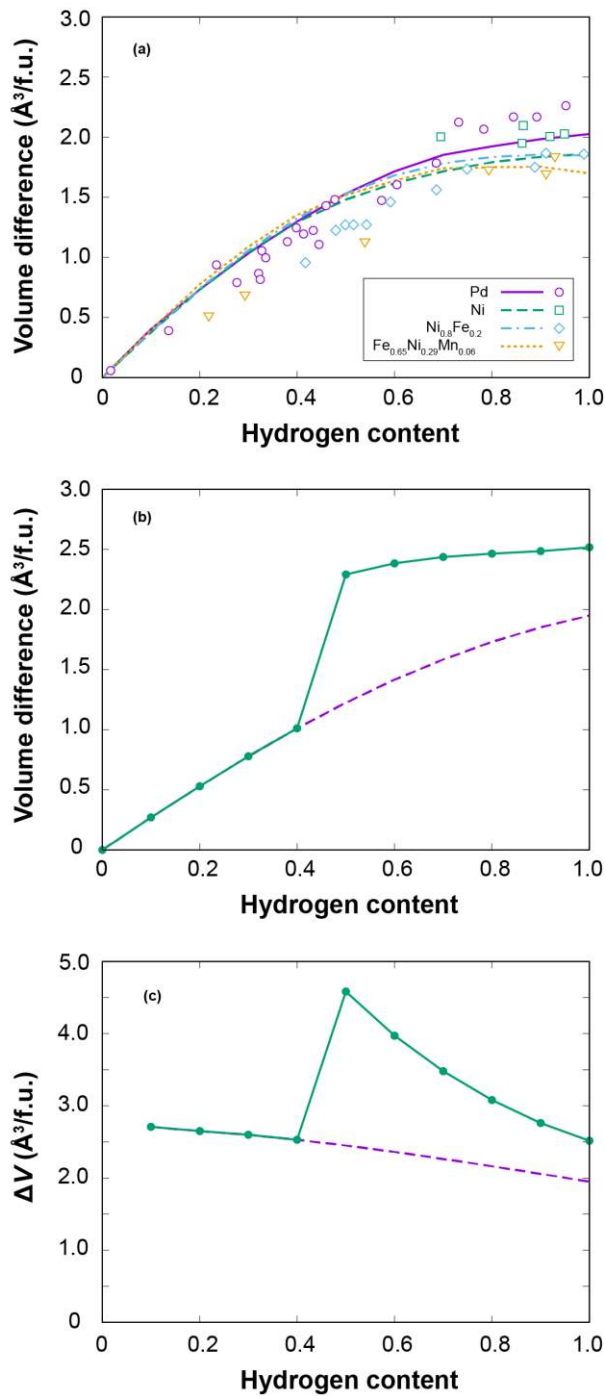
669



670

671 **Fig. 2.** (a) Compression curves of dhcp FeH and hcp Fe. Blue broken line indicates
 672 ferromagnetic dhcp FeH. Blue and black solid lines are non-magnetic dhcp FeH and hcp
 673 Fe, respectively. Previous DAC measurements (open square; Hirao et al. (2004), filled

674 square: Pépin et al. (2014), open circle: Fei et al. (2016), filled circle: Dewaele et al.
675 (2006)) are also shown for comparison. (b) Curie temperature of dhcp FeH. (c) Stable
676 crystal and magnetic structure of FeH_x as function of pressure at given hydrogen content.
677 Note that we only considered following four phases: ferromagnetic dhcp, nonmagnetic
678 dhcp, ferromagnetic hcp and nonmagnetic hcp. We also neglect the phase separation,
679 which may occur at low temperature.
680



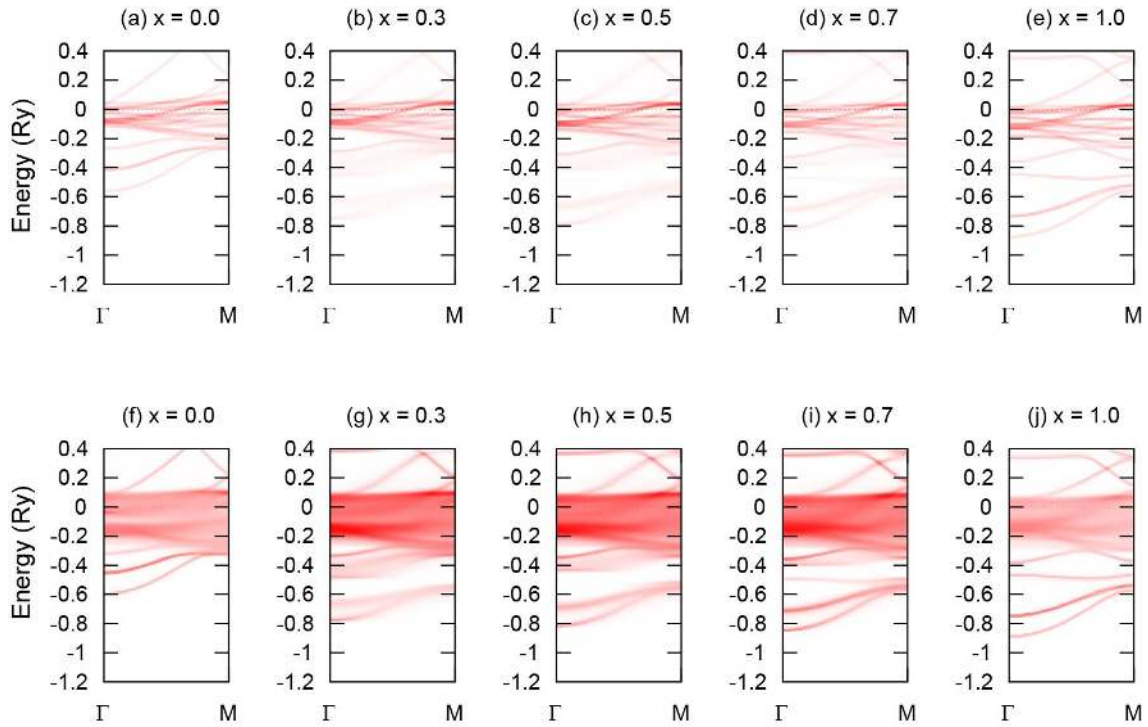
681

682 **Fig. 3.** Increase of volume of metal-hydrogen alloys as functions of hydrogen content, x .

683 (a) fcc metal-hydrogen alloys at ambient pressure. Our first-principles results (purple

684 solid line: Pd, green dashed line: Ni, blue dotted-dashed line: $\text{Ni}_{0.8}\text{Fe}_{0.2}$, yellow dotted

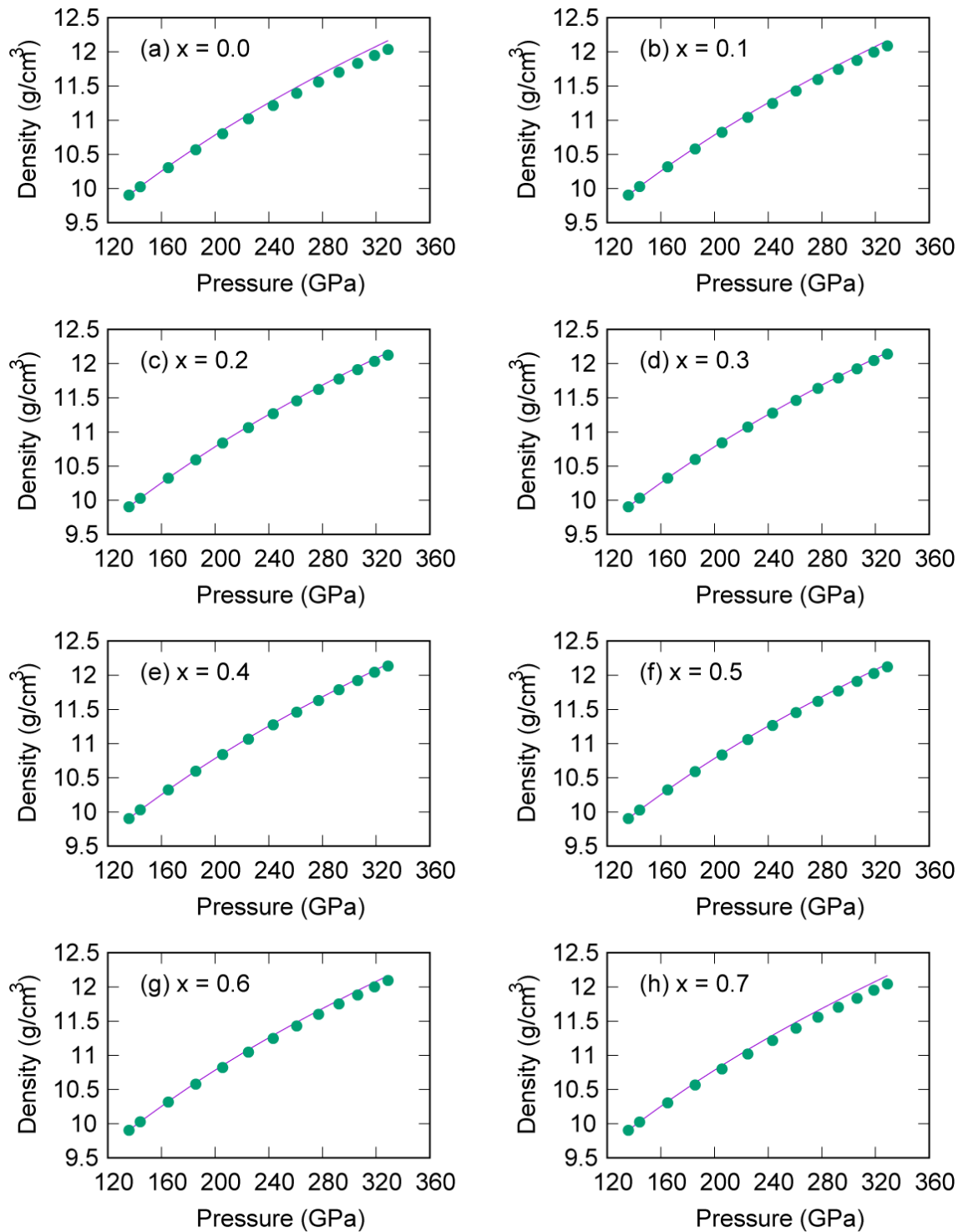
685 line: $\text{Fe}_{0.65}\text{Ni}_{0.29}\text{Mn}_{0.06}$) are consistent with previous experiments (purple circle: Pd,
686 green square: Ni, blue diamond: $\text{Ni}_{0.8}\text{Fe}_{0.2}$, yellow triangle: $\text{Fe}_{0.65}\text{Ni}_{0.29}\text{Mn}_{0.06}$) (Fukai,
687 2006). (b) FeH_x alloys at 20 GPa. Green solid line with circle indicates FeH_x of stable
688 phase, whereas purple broken line represents FeH_x in non-magnetic state. Note that
689 magnetic transition violates the linear volume-hydrogen content relation, which
690 observed in nonmagnetic FeH_x and many fcc metal-hydrogen alloys. (c) The $\Delta V_{\text{H}} =$
691 $(V_{\text{FeH}_x} - V_{\text{Fe}}) / x$ of FeH_x at 20 GPa.
692



693

694 **Fig. 4.** Electronic band structures of dhcp FeH_x alloys at $V = 90 \text{ Bohr}^3/\text{f.u.}$ (a) to (e) are
 695 non-magnetic states with $x = 0.0, 0.3, 0.5, 0.7,$ and $1.0,$ respectively. Similarly, (f) to (j)
 696 are LMD states. Note that the broadening due to the chemical disorder of interstitial
 697 hydrogen is observed mainly at around $-0.6 \text{ Ry},$ whereas the broadening due to the
 698 magnetic disorder is significant at the vicinity of the Fermi level.

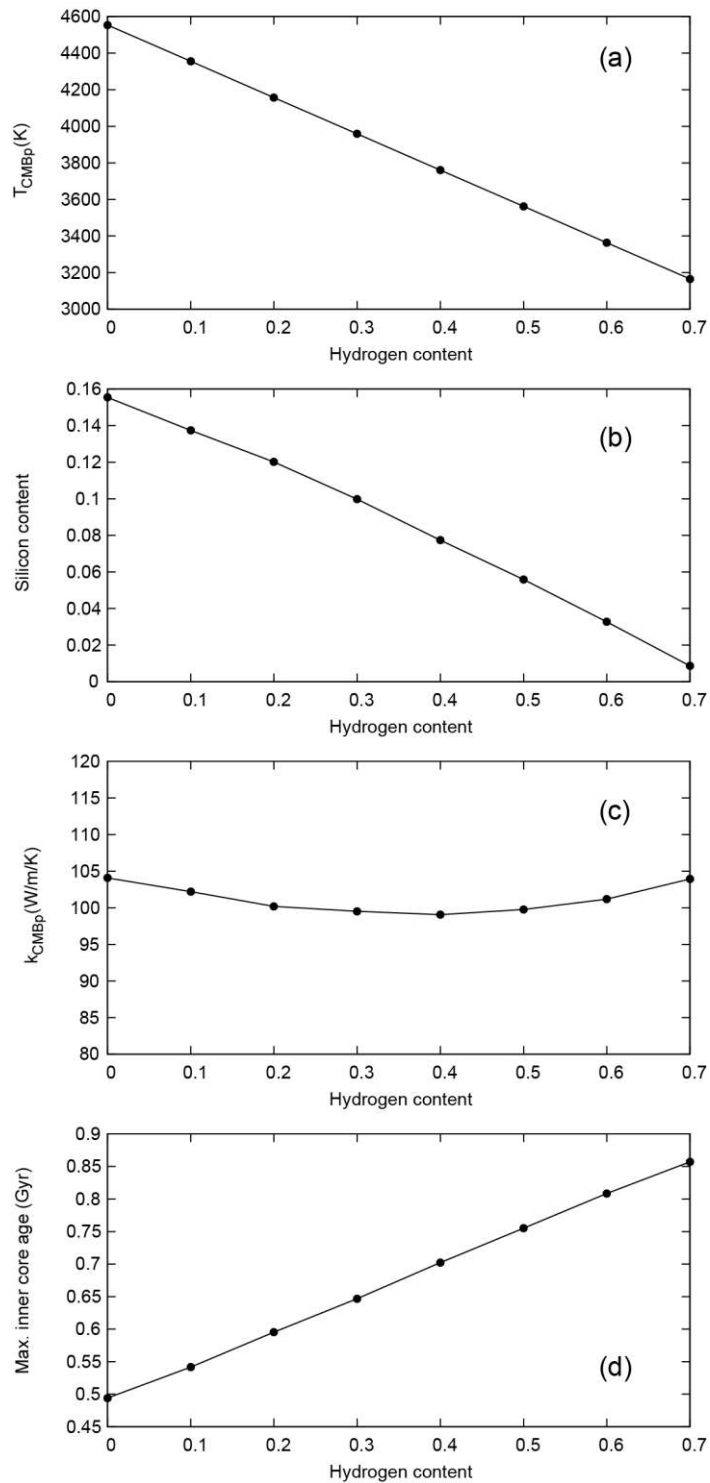
699



700

701 **Fig.5.** The PREM (green circle) and the calculated (purple line) density from the
 702 equation of states of $\text{Fe}_{1-y}\text{Si}_y\text{H}_x$ alloys. The Si contents are determined so that the density
 703 of the alloy match the density of PREM at the CMB.

704



705

706 **Fig. 6.** Modeling results of $\text{Fe}_{1-y}\text{Si}_y\text{H}_x$ ternary core as function of hydrogen content, x .

707 (a) Present-day CMB temperature. (b) Silicon content, which match the PREM density

708 at the CMB. (c) Present-day CMB thermal conductivity. (d) Maximum inner core age.

